JOURNAL OF MATERIALS SCIENCE **34** (1999) 4909–4920

The crack tip strain field of AISI 4340

Part I *Measurement technique*

N. N. KINAEV[*,‡], D. R. COUSENS[‡], A. ATRENS[*,§]
[*] *Department of Mining, Minerals and Materials Engineering, The University of Queensland, Brisbane, QLD, 4072*
[‡] *Centre for Microscopy and Microanalysis, The University of Queensland, QLD, 4072*
E-mail: atrens@minmet.uq.oz.au

This is the first paper in a study on the influence of the environment on the crack tip strain field for AISI 4340. A stressing stage for the environmental scanning electron microscope (ESEM) was constructed which was capable of applying loads up to 60 kN to fracture-mechanics samples. The measurement of the crack tip strain field required preparation (by electron lithography or chemical etching) of a system of reference points spaced at $\sim$5 μm intervals on the sample surface, loading the sample inside an electron microscope, image processing procedures to measure the displacement at each reference point and calculation of the strain field. Two algorithms to calculate strain were evaluated. Possible sources of errors were calculation errors due to the algorithm, errors inherent in the image processing procedure and errors due to the limited precision of the displacement measurements. Estimation of the contribution of each source of error was performed. The technique allows measurement of the crack tip strain field over an area of 50×40 μm with a strain precision better than ±0.02 at distances larger than 5 μm from the crack tip.

1. Introduction

Stress corrosion cracking (SCC) [1] is a complex multistep process which involves the combination of mechanical, physical and chemical processes that accomplish the separation of bonds at the initiation site or at the crack tip, thereby initiating or advancing the SCC crack. SCC often occurs under corrosive conditions where general corrosion is not a problem. The corrosion resistance of interest is caused by surface films that separate the material from its environment. Such films can cause a low rate of general corrosion despite a large thermodynamic driving force for corrosion. For example, stainless steels are stainless because of a very thin passive surface layer which is essentially Cr_2O_3. Although, this layer is so thin (passive layers are typically less than 4 nm, [2–5]) that it cannot be seen with the naked eye, this layer is nevertheless effective in separating the steel from its environment. The passive films on stainless steels are usually self repairing. The breakdown of such films can be induced chemically (e.g. by chlorides), and pitting corrosion results when the breakdown is localised. Localised film breakdown under the joint action of a stress and an environment is the essence of SCC even when the mechanism of crack advance involves hydrogen. Cracking of surface films has been shown to be involved for SCC initiation in pipeline steels [6, 7] and high strength steels [8–10].

Stress rate effects have been shown [11–14] to be an important part of the SCC mechanism, and in particular crack tip creep has been shown to be important part of the SCC mechanism for high strength steels undergoing SCC in water, which can provide an explanation for the stationary cracks observed in service. Room temperature creep has been measured for high strength steels including AISI 4340 and AerMet100 [15].

The development and application of micro-measurement technology is required to advance our knowledge of the processes occurring during SCC. Detailed observations and measurements are needed down to the atomic level to understand the issues involved in particular the influence of stress and strain on crack advance. A possible step in the direction of appropriate micro-measurement technology may be provided by measurements of the crack tip strain field using the environmental scanning electron microscope (ESEM) [16].

Several techniques for strain mapping have been described in the literature [17–20]. The general approach is to measure displacements of reference points on the sample surface and to calculate the strain at each point from the experimentally obtained displacement field. Obtaining strain data in the vicinity of a crack tip requires a high spatial resolution, of the order of micrometres. This spatial resolution can be obtained using scanning electron microscopy (SEM) [17]. The key requirements for the strain mapping technique are: (1) a loading stage to apply a load to a suitable specimen inside a scanning electron microscope; (2) a system of

§ Author to whom all correspondence should be addressed.

reference points on the sample surface; (3) an image processing procedure to allow measurement of the displacement of each reference point, and (4) an algorithm to calculate the strain field from the displacement data.

Several loading stages have been described in the literature [21, 22]. They are mostly hydraulic and all require the use of relatively small samples. Thus, they are not suitable for full-size fracture-mechanics samples.

Several systems of reference points have been described in the literature [18–20, 23–25]. Attwood and Hazzledinene [23] developed an electron lithography technique to produce a regular grid on the sample surface. This technique with different modifications has been used by several research groups [18–20]. It produces a good reliable system of reference points. However it covers a relatively small area of the sample. Electron lithography is most convenient if there is a programmable control unit to automatically produce the grid by movement of the electron beam or sample stage. Without such a control unit this technique is very time consuming. Davidson [25] and Franke *et al*. [24] used microstructural features of the sample produced by light chemical etching of the sample surface. Sample preparation is easy but there are significant problems in image processing.

Several algorithms are available for calculation of the strain from the discrete displacement data. The simplest approach is to calculate the engineering strain e, as $e = \Delta l/l$, where l is the distance between two reference points on the unstrained sample and Δl is the difference in that distance between the strained and unstrained sample [19]. Other approaches [17, 18, 26, 27] have been based on the calculation of the partial derivatives of the displacements with respect to coordinates at each reference point using cubic interpolation of the displacement data. Alternatively the partial derivatives have been calculated by estimation of an average displacement gradient tensor using integration of the displacements over a volume element [18]. Knowledge of the partial derivatives at each grid point allows calculation of the corresponding strain values. However, the rigorous estimation of the accuracy and precision of these algorithms has not been reported.

This paper is the first in a series of papers in a study of the influence of different environments on the strain field at the crack tip in AISI 4340 high strength steel. It describes the experimental procedure used in these studies.

2. Experimental

2.1. Sample geometry and load calibration

A bolt-loading standard DCB sample geometry was used as illustrated in Fig. 1. This geometry allows *in situ* ESEM experiments to be compared directly with *ex situ* experiments. A major advantage of the bolt-loading configuration was the simplicity of implementation in an electron microscope. The stress intensity factor was calculated using Equation 1 [29]:

$$K_I = \frac{Pa}{BH^{1.5}\sqrt{1000}}\left(3.46 + 2.38\frac{H}{a}\right), \qquad (1)$$

where K_I is the stress intensity in MPa$\sqrt{\text{m}}$, P is the load in N applied to the specimen, a is the crack length, B the specimen thickness in mm and H is the half-width of the sample in mm. The applied load was measured from the crack mouth opening displacement (CMOD) and a compliance calibration of the sample. The empirical equation connecting the CMOD, crack length and applied load was found to be

$$\frac{\delta_{\text{m}} BE}{P} = \left(-48.644\left(\frac{a}{W}\right)^3 + 973.3497\left(\frac{a}{W}\right)^2 - 420.6244\left(\frac{a}{W}\right) + 101.2893\right), \qquad (2)$$

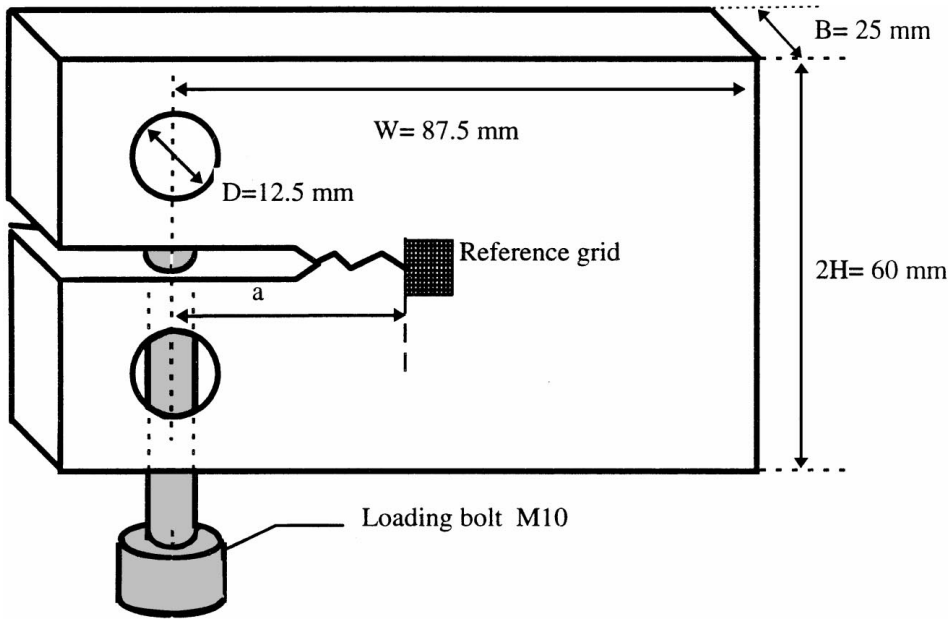

Figure 1 Sample geometry.

where δ_m is CMOD in mm, E is the Young's modulus in MPa, W is the length of the sample in mm and a/W is the dimensionless crack length. The crack mouth opening was measured with a commercial CMOD gauge attached by knife edges to both sides of the crack.

2.2. Loading stage

The loading stage was manufactured to allow experiments in the ESEM "Electroscan E-3" as illustrated in Fig. 2. The design criteria were: (1) the ability to apply the required load to the sample quickly, (2) the ability

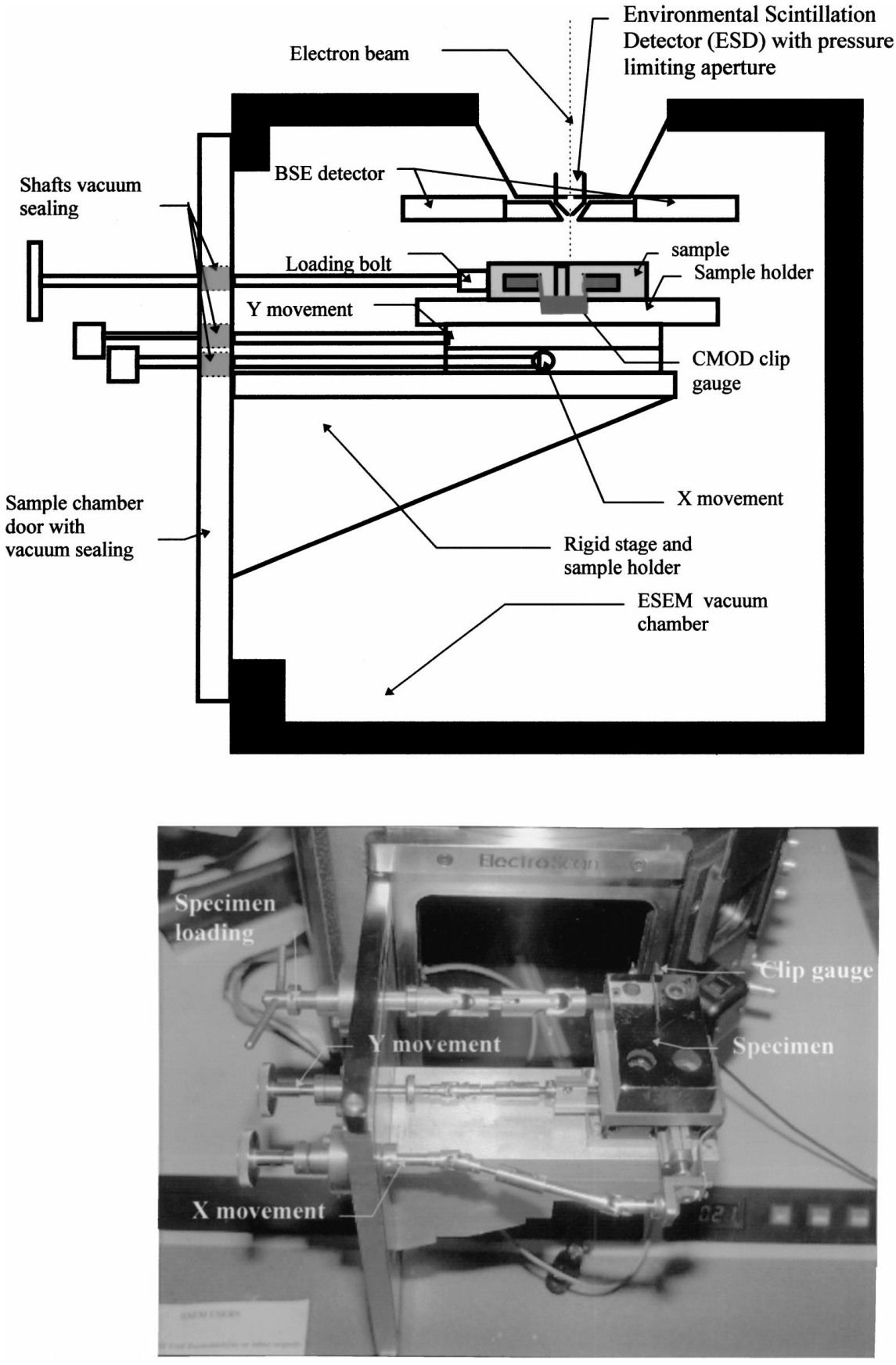

Figure 2 Schematic drawing and general view of the loading stage for the ESEM "Electroscan-3".

to monitor the applied load, (3) the ability to use heavy samples without vibrations, and (4) the ability to control sample movement with high positioning precision.

The loading stage was mounted on the sample chamber door of the microscope. To minimise vibration, the sample holder was placed on a rigid aluminium plate reinforced by a triangular support. A system of sliding shafts and bevel gears, connected to the moving parts of the sample holder, allowed external control of the X and Y movement of the sample. The sample could be moved over an area of ± 12.5 mm in the X-X and Y-Y directions with a positioning precision of approximately ± 1 μm. All the shafts for the stage movement and sample loading were connected to the inner volume of a microscope sample chamber through rotational vacuum seals and were moved manually. A motor for the sample loading could be easily added. The loading stage was suitable for samples with a mass of the order of 1 kg. No vibration of the sample was observed during the experiments using DCB samples weighing 1.1 kg.

The sample was loaded by a system of shafts and universal joints connected to the sample loading bolt. As the sample loading bolt screws down into the specimen, it pushes the sample apart (Fig. 3). The loading conditions can be considered to a first approximation as constant deflection Mode I loading. This sample loading provided a loading precision of ± 0.5 MPa $\sqrt{}$m with the ability to manually load the sample up to 45 MPa $\sqrt{}$m within 5–10 s.

The conventional ESEM gas scintillation secondary electron detector cannot operate in the absence of a gaseous environment [16]. A scintillation BSE detector was developed for the ESEM [28] to operate in both high vacuum and various gaseous environments. In combination with this detector, the loading stage allows experiments to be performed in (1) high vacuum, as a conventional SEM, and (2) in water vapour or hydrogen at pressures up to 2.7 kPa (20 Torr).

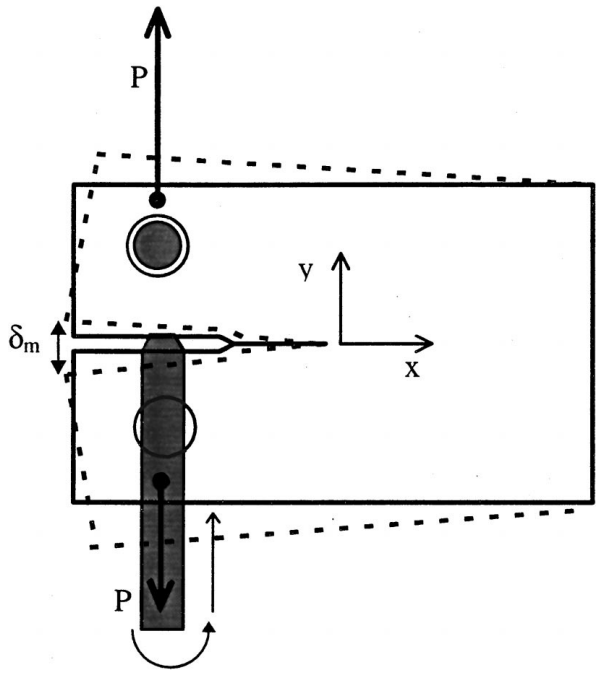

Figure 3 Sample loading and coordinate system.

This stage does not allow performance of cyclic experiments, unlike the ones described by [22, 23]. However it has advantages compared with existing stages in terms of a larger sample size (DCB sample of $60 \times 20 \times 100$ mm in comparison with the maximum 20 mm wide samples for that of [22]), and a larger applied load (60 kN in comparison with a possible maximum load of 4.4 kN for that of [22]).

2.3. Sample preparation

Samples of AISI 4340 steel were machined, austenitised at 870 °C for 3 h and quenched into agitated oil. To remove the decarburised layer after the heat treatment they were surface ground to remove 2 mm. Sample hardness after quenching was in the range of 50–55 RC. After quenching, the amount of retained austenite as measured by X-ray diffraction did not exceed 2–3%.

Fatigue pre-cracking was carried out in an "Instron 1342" hydraulic tensile testing machine with an applied stress intensity factor cycling between a slightly positive value and a maximum value in the range of 10–12 MPa$\sqrt{}$m, so that $\Delta K \leq 7$MPa$\sqrt{}$m at a frequency of 50 Hz.

Strain mapping requires a system of reference points, on the sample surface in order to allow determination of the displacement field in the crack tip area. The reference system should satisfy the following criteria. It should not change the mechanical properties of the material surface; e.g. scratches could introduce stress concentrators at the sample surface. The reference system should adhere to the sample surface. It should provide sufficient contrast to be easily detectable. There should be enough reference points to perform the strain mapping in the crack tip area.

Two alternative systems of reference points were used. A grid was produced by a direct electron beam lithography technique as illustrated in Fig. 4a. Natural microstructural features were used as reference points as illustrated in Fig. 4b.

To prepare the reference grid, the sample was polished to a mirror finish and washed in hexane and acetone in an ultrasonic bath. A thin layer of partly polymerised polymethylmethacrylate (PMMA) was deposited on the surface in a centrifuge at 3000 rpm. Polymerisation of the PMMA film was completed in vacuum furnace at 120 °C for 12–16 h. The PMMA film thickness was not measured directly, but the thickness was considered acceptable if it produced a green interference colour. This indicated a film thickness of approximately 250 nm. Orthogonal grid lines were drawn using the electron beam in the line-scan mode in the ESEM under high vacuum conditions. Optimal conditions for electron lithography in the ESEM "Electroscan-E3" were found to be: an electron beam energy of 15–20 keV; condenser lens setting (for the LaB_6 filament) of 30, corresponding to a beam current of about 10–20 nA; line scan time of 26 s/line. The sample was washed in the acetone to remove the unexposed PMMA. The unexposed area dissolved fully, while the exposed lines then formed a polymer grid on the surface.

This method worked well, but had the disadvantage of dimensions limited to about 80×80 μm due to the

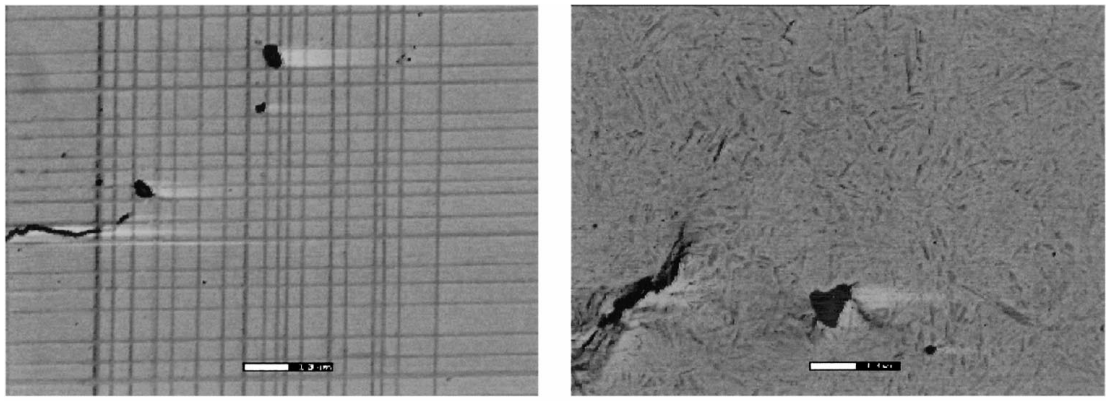

Figure 4 Examples of the reference point systems: (a) reference grid produced by electron beam lithography; (b) natural features produced by a light chemical etching of the sample surface. Scale bar is equal to 10 μm.

limited area of electron beam scan in the ESEM "Electroscan E3." At large loads, the crack frequently propagated beyond the area covered by the grid.

The second approach was to use natural features on the sample produced by light etching after polishing using a 5% solution of picric acid in ethanol for 20 s. The natural features reference system provided a much larger area in a very short time. However there was greater difficulty in image processing.

2.4. ESEM operation

For experiments in a high vacuum environment, the sample was inserted into the ESEM, which had been previously fitted with the BSE detector. Images of the crack tip area were obtained in composition contrast mode. They were digitally captured with the Digital Micrograph Image Acquisition System. The image capture board was connected directly to the video amplifier output/monitor input of the ESEM and was able to provide a 640 $\times$ 480 pixel image with 256 grey levels.

The loading schedule is illustrated in Fig. 5. The sample was loaded to the desired load within 5–10 s. A fast loading rate was necessary to minimise time for creep during loading. Then images of the crack tip area were captured on the computer at times equal to 1, 2.5, 5, 10, 15, 30, 45 and 60 min after sample loading. The crack tip strain field was calculated as discussed subsequently from these images compared with initial unstrained image.

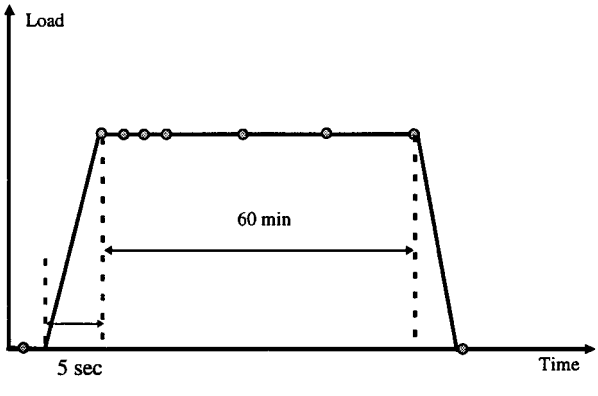

Figure 5 Loading schedule for the experiments.

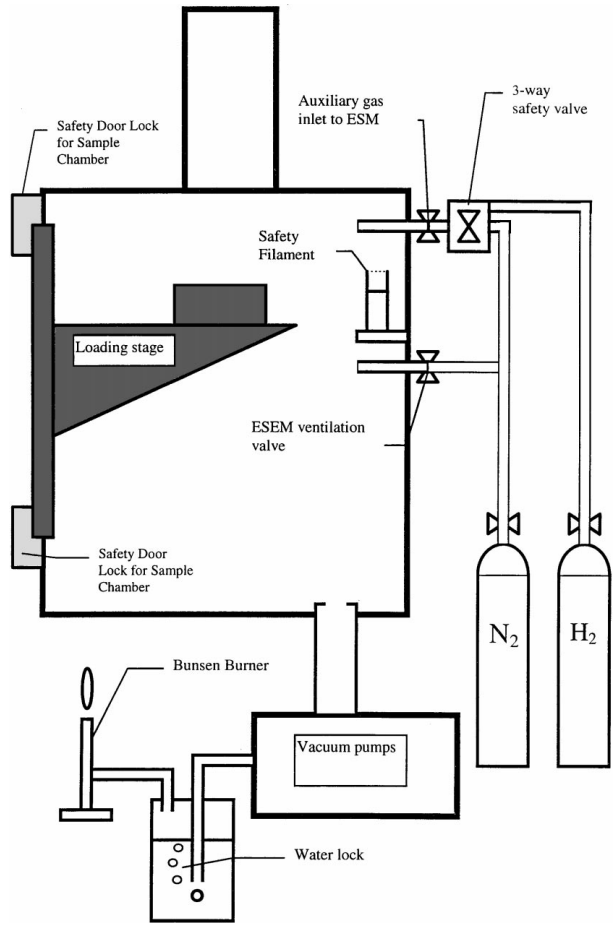

Figure 6 Experimental setup for the ESEM experiments in hydrogen.

For experiments in a hydrogen environment, the standard gas scintillation ESD detector was used. The ESEM vacuum system was modified as illustrated in Fig. 6 [30]. The auxiliary gas inlet of the ESEM was connected to a 3-way safety solenoid valve. The normally open inlet of the safety valve was supplied with the inert gas N_2. The normally closed inlet was connected to the hydrogen supply. This valve provided automatic switching to the inert gas in case of an unexpected power failure. The vent gas valve of the ESEM was connected to the nitrogen gas supply to prevent accidental access of oxygen to the sample chamber. To prevent oxygen build up in the sample chamber, a safety

filament heated by a battery was placed near the gas entrance in the sample chamber. To eliminate hydrogen from the exhaust of the pumping system, and to prevent build up of hydrogen in the laboratory, the exhaust from the vacuum pumps was connected through a manifold and water lock to a Bunsen burner.

The ESEM was flushed with nitrogen after the sample had been introduced into the microscope to reduce the partial pressure of residual oxygen. The sample was then exposed to hydrogen at a pressure of 5 Torr for at least 2 h to ensure steady state of hydrogen sorption onto the sample surface. Immediately after the specimen was exposed to hydrogen, the brightness of the ESD signal increased as hydrogen was adsorbed on the specimen surface. The pressure control system of the ESEM, which has been designed for controlling water vapour pressure, was not ideal for controlling the hydrogen pressure. There was a small instability in the hydrogen pressure in the ESEM sample chamber for the first 2 h. The lower ionisation potential of hydrogen compared to water caused the ESD signal in hydrogen to be more sensitive to pressure changes than in the standard case of a water vapour environment. Thus, this period of preliminary exposure was also necessary to stabilise the working conditions of the ESEM with respect to the contrast and brightness of the ESD signal. The stabilisation of the signal from the ESD detector indicated that the sample surface was saturated with hydrogen and that the hydrogen pressure inside the chamber was remaining constant. After 2 h of exposure to hydrogen, the sample was loaded to the desired stress intensity factor in 10–15 s and maintained at that load for up to 6.5 h. The images of the crack tip area were taken at times equal to 6, 10, 15, 30, 60, 90, 120, 300 and 390 min after loading. Then the hydrogen environment was replaced by water vapour and the samples were left in water vapour at 15 Torr (approx. 75% relative humidity) for about 9 h.

2.5. Displacement measurements

The image processing sequence is illustrated in Fig. 7. The captured image (Fig. 7a) was subjected to nonlinear adjustment of contrast and brightness (Fig. 7b). Laplacian edge filters were applied to enhance the grid or features (Fig. 7c). The points of interest were manually selected (Fig. 7d). For the reference grid, the intersections of grid lines (usually polygons of about 3 by 4 pixels) were considered as reference points. In the case of the natural features reference system, the choice of reference points was performed by visual comparison between the strained and the initial images. Features with the same shape and similar surroundings were selected. When the images contained an excessive number of features it was difficult to find the same feature on different images. On the other hand, when a small number of features were present it was not possible to select a sufficient number of reference points. Image processing up to the selection of reference points was performed with "Adobe PhotoShop" with the Image Processing Tool Kit. The images of the selected reference points (either intersections of the grid lines or marks on the boundaries of selected microstructural features) were imported into either the "Image Tool" or the "NIH Image" software package (Fig. 7e) for automatic determination of the coordinates of each reference point by standard plug-ins (e.g. "Object Analysis"). The image acquisition system provided an image of 640 × 480 pixel. At a magnification of 1000 times, this corresponds to a distance of 0.22–0.25 μm per pixel. The coordinate of the centroid of each reference point was used as the exact position of the reference point. Since each reference point corresponded to 3–4 pixels, coordinates could be measured with a precision of approximately ±0.15 μm, which is slightly better than single pixel size.

The major disadvantage of this procedure was the choice of features which were sometimes on the edge of visibility. The choice of features by the operator introduced some subjectivity. To minimise this subjective factor and to increase the reliability of the measurements, the whole measurement procedure was repeated 3 times for each image and the average of these three independent measurements was used as the reference point coordinate.

3. Strain calculation

The scale of the measurements for strain mapping in the crack tip area excluded the use of strain gauges. The only measurable quantities were the displacements of the reference points u and v (along x- and y-axes, respectively) (Fig. 8). Consider the polygon of N reference points as shown in Fig. 9. The strain over this sub-grid was assigned to the centroid P_0 with coordinates $(\frac{1}{n}\sum_i^n x_i, \frac{1}{n}\sum_i^n y_i)$, where x_i and y_i are the coordinates of the ith point of the sub-grid (Fig. 9). Strain was calculated from the displacement data in two ways.

The first approach was based on the simple definition of engineering strain as

$$e_{yy} = \frac{1}{n}\sum_{i=1}^{n} \frac{(y_i^0 - y_{i+1}^0) - (y_i^s - y_{i+1}^s)}{(y_i^0 - y_{i+1}^0)}, \qquad e_{xx} = \frac{1}{n}\sum_{i=1}^{n} \frac{(x_i^0 - x_{i+1}^0) - (x_i^s - x_{i+1}^s)}{(x_i^0 - x_{i+1}^0)} \tag{3}$$

where $y_i^0, x_i^0, y_i^s, x_i^s$ were the x and y coordinates of the ith point of the initial and strained grid, and n was the number of the points used for averaging the data. In the present case $n = 8$. Averaging was necessary to minimise the calculation error due to the error in the coordinate measurements.

The second approach used the following equations [26]:

$$\left.\begin{aligned} \varepsilon_{xx} &= \sqrt{1 + 2\eta_{xx}} - 1 \\ \varepsilon_{yy} &= \sqrt{1 + 2\eta_{yy}} - 1 \\ \gamma_{xy} &= \sin^{-1}\left(\frac{2\eta_{xy}}{\sqrt{1 + 2\eta_{xx}}\sqrt{1 + 2\eta_{yy}}}\right) \end{aligned}\right\} \tag{4}$$

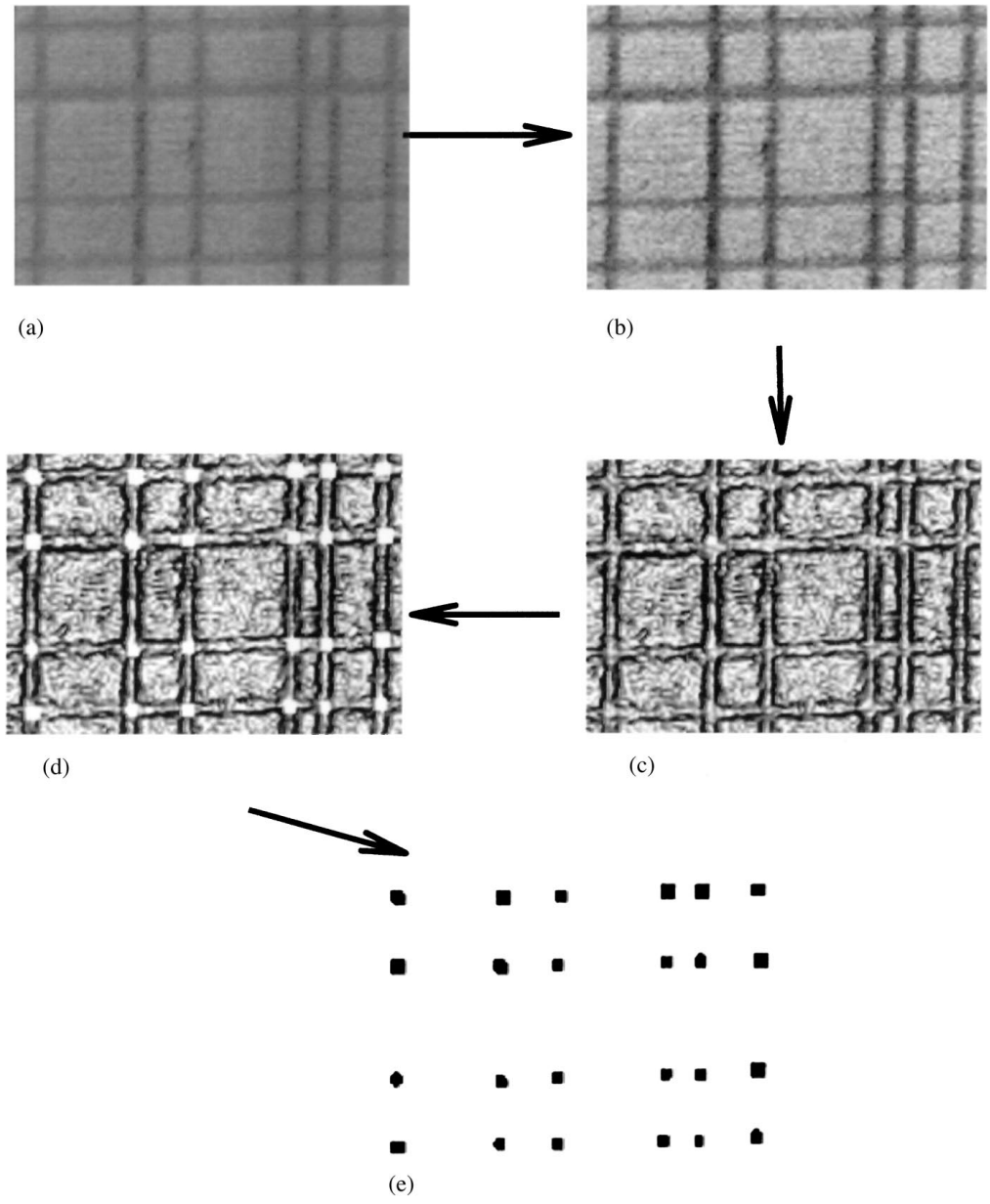

Figure 7 Image processing sequence: (a) initial image, (b) after adjustment of brightness and contrast, (c) after applying a Laplacian edge filter, (d) the selected reference points, (e) image of the selected reference points ready for automatic determination of the coordinates. Illustrated with the example of grid reference system (Fig. 4a).

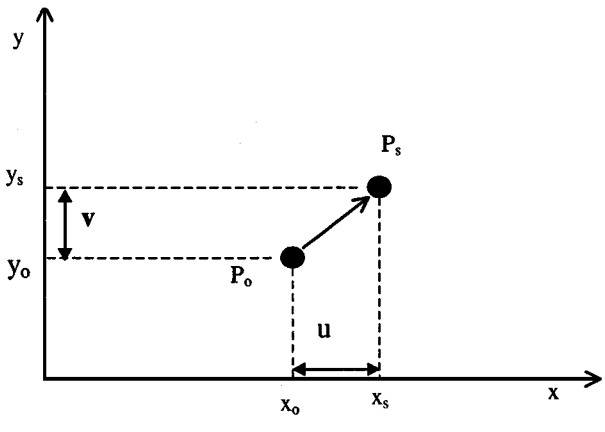

Figure 8 Definition of the displacements. P_0 is the initial position of reference point; P_s is the position of the same point after loading.

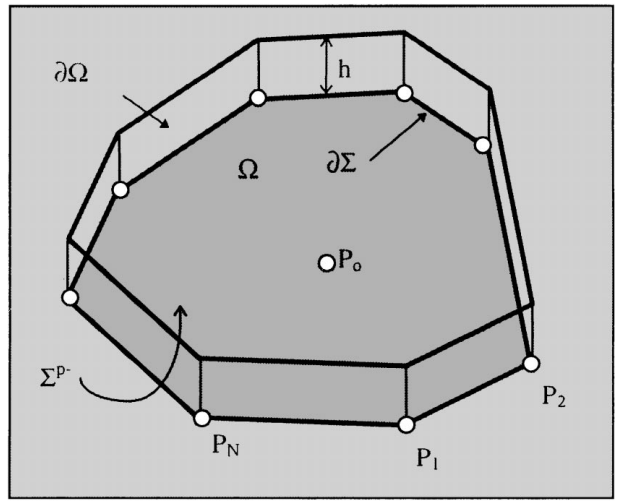

Figure 9 Local strain computations.

where:

$$\left.\begin{aligned} \eta_{xx} &= u_{,x} + \frac{1}{2}\left[u_{,x}^2 + v_{,x}^2\right] \\ \eta_{yy} &= v_{,y}^2 + \frac{1}{2}\left[u_{,y}^2 + v_{,y}^2\right] \\ 2 \cdot \eta_{xy} &= u_{,y} + v_{,x} + u_{,x}u_{,y} + v_{,x}v_{,y} \end{aligned}\right\} \quad (5)$$

and $u_{,x}$, $u_{,y}$, $v_{,x}$ and $v_{,y}$ are the notations for $\partial u/\partial x$, $\partial u/\partial y$, $\partial v/\partial x$, $\partial v/\partial y$.

The error of the strain calculations is proportional to the error of the determination of the partial derivatives $u_{,x}$, $u_{,y}$, $v_{,x}$ and $v_{,y}$. Thus, the determination of these partial derivatives is critical for the accuracy of strain mapping.

Mathematically, the problem can be described as the estimation of the partial derivatives of an unknown function, given as a discrete set of values at the reference points. The algorithm for this estimation must satisfy the following requirements. (1) There is no preliminary knowledge about the partial derivatives. (2) The values of the partial derivatives, and thus strain values, should be invariant with respect to the origin of the coordinate system, i.e. the values of partial derivatives should be independent of the choice of the origin of the coordinate system. (3) The algorithm should be stable to the random measurement errors of the displacement values. (4) The algorithm should be independent of the shape of the grid. That is, the same strain should be calculated for the cases of an irregular grid, a curvilinear grid or a set of random points.

Two major approaches to the estimation of the partial derivatives from the displacement data have been described in the literature. The first approach [24, 26] divided the grid into subgrids, performed a bicubic interpolation of the displacement data and calculated the partial derivatives for each point from the parameters of the bicubic interpolation. The second approach [18], was based on the estimation of the average displacement gradient tensor using integration of the displacements over a volume element. This second approach has been adopted and modified in the present work. This approach has a potential advantage that the inherent averaging of the displacement data in this algorithm would minimise the effect of measurement errors.

The main scheme of the algorithm was as follows. Consider the point P_0, which is the centroid of a polygon Σ^- defined by N reference points P_i, numbered anticlockwise, as shown in Fig. 9. The polygon Σ^- is the bottom surface of the domain Ω. The domain Ω is a prism with an arbitrary small height h, bounded on top and bottom surfaces by Σ^+ and Σ^-. V is the volume of Ω, $\partial\Omega$ is the regular edge of Ω, S is the area of the Σ^- or Σ^+, $\partial\Sigma$ is the boundary of Σ^+ and ν is the normal to the outer surface for all parts of the surface of Ω. Let $\mathbf{X}^0$ (x^0, y^0) and $\mathbf{X}^S$ (x^s, y^s) be vectors pointing to the position P_0 and P_s of the reference point of the initial and deformed grid respectively. The algorithm as described by Allais *et al.* [18] used the deformation gradient $\mathbf{F}' = \frac{\partial \mathbf{X}^S}{\partial \mathbf{X}^0}$. This choice leads to a set of final equations which are dependent of the choice of coordinate origin, violating the second requirement that the algorithm be independent of the choice of the coordinate origin. To eliminate this violation the deformation gradient was replaced by the displacement gradient. This replacement ensures that the final set of equations to calculate strain are independent of the choice of the coordinate origin.

The displacement gradient is given as

$$\mathrm{F} = \left.\frac{\partial \mathbf{U}}{\partial \mathbf{X}}\right|_{\mathbf{X}=\mathbf{X}^0} = \left.\begin{bmatrix} u_{,x} & v_{,x} & w_{,x} \\ u_{,y} & v_{,y} & w_{,y} \\ u_{,z} & v_{,z} & w_{,z} \end{bmatrix}\right|_{x=x^0, y=y^0, z=z^0} \quad (6)$$

where

$$U = \begin{pmatrix} u \\ v \\ w \end{pmatrix} = X^0 - X^s = \begin{pmatrix} x^0 - x^s \\ y^0 - y^s \\ z^0 - z^s \end{pmatrix}$$

The displacement gradient for the point P_0 averaged over Ω can be estimated as

$$\mathbf{F}\|_{\mathrm{P}=\mathrm{P}_0} = \langle \mathbf{F} \rangle \frac{1}{V} = \int_\Omega \mathbf{F}\, d\omega, \quad (7)$$

were $d\omega$ is a volume element. Transformation of the volume to the surface integral using Green's formula [18] gives

$$\langle \mathbf{F} \rangle = \frac{1}{V} \int_{\partial\Omega} \mathrm{U} \otimes \nu\, ds, \quad (8)$$

where ν is the outer normal to the edge of Ω and ds is the surface element. In the terms defined above and in Fig. 9, this becomes a sum of a curvilinear integral over the polygon boundary $\partial\Sigma$ and surface integrals over the upper and lower surfaces Σ^+ and Σ^-:

$$\frac{1}{V}\int_{\partial\Omega} \mathbf{U} \otimes \nu\, ds = \frac{1}{S}\left(\int_{\partial\Sigma} \frac{\int_h \mathbf{U}\, dh}{h} \otimes \nu\, dl + \frac{\int_{\Sigma^+} \mathbf{U}\, ds - \int_{\Sigma^-} \mathbf{U}\, ds}{h} \otimes \nu \right) \quad (9)$$

where dl is the length element of the boundary $\partial\Sigma$.

The mathematical transformations described in detail by Allais *et al.* [18], based on the assumption that the strain only occurs in the x-y plane. Therefore h is tending to 0 and Equation 9 can be transformed as $\frac{1}{V}\int_{\partial\Omega} \mathbf{U} \otimes \nu\, ds = \frac{1}{S}(\int_{\partial\Sigma} \mathbf{U} \otimes \nu\, dl + \partial \int_\Sigma \mathbf{U}\, ds/\partial\nu_\Sigma \otimes \nu)$. The surface of the sample is perpendicular to the observation axis Z. If $\mathbf{e}_Z$ is the unit vector along direction Z, then the components of the tensor $\mathbf{F}$ in the Cartesian coordinates would be $\mathbf{F}_{ij} = \frac{1}{S}(\int_{\partial\Sigma} u_i\, \nu_j\, dl + \frac{\partial \int_\Sigma u_i\, ds}{\partial \nu_\Sigma}(\mathbf{e}_Z)_j)$. For $j \neq Z$, $(\mathbf{e}_Z)_j$ vanishes, thus $\mathbf{F}_{ij}(j \neq Z)$ vanishes. Since we cannot measure displacements in the Z direction, u_Z is unavailable, therefore $\mathbf{F}_{Zj}$ can not be computed. For $i \neq Z$ and $j \neq Z$ the OXY components of $\mathbf{F}_{ij}$ can be written as $\mathbf{F}_{ij} = \frac{1}{S}\int_{\partial\Sigma} \mathbf{U} \otimes \nu\, dl$. Another important assumption is that $\mathbf{U}$ varies linearly from one vertex of segment $\partial\Sigma$ to the other and $\nu\, dl$ is constant on a segment. This assumption is valid only for small distances between the polygon points. N is the number of the vertices of the considered polygon P, $\mathbf{U}^n$ are the displacements of the nth point, ν^n is the outer normal to the

segment between dots n and $n+1$ and dl^n is the length of this segment. Therefore the in-plane components of the tensor are equal to $\mathbf{F}_{ij} = \frac{1}{2S}\sum_{n=1}^{N}(\mathbf{U}^n + \mathbf{U}^{n+1}) \otimes \nu\, dl$ where i is cyclic with period N, i.e. when $i = N$, $i+1$ is equal to 1. Assume, that the segments of $\partial\Sigma$ belong to OXY plane, therefore, ν^n also belong to the same plane. If vertices of polygon numbered counterclockwise, then the array of components of $\nu^n dl^n$ is equal to

$$[\nu^n dl^n] = \begin{bmatrix} y^0_{n+1} - y^0_n \\ -x^n_{n+1} + x^n_n \\ 0 \end{bmatrix}.$$

The transformations yield the following formulas:

$$\begin{cases} \mathbf{F}_{xx} = u_{,x} = \dfrac{1}{2S}\displaystyle\sum_{n=1}^{N}(u_i + u_{i+1})\big(y^0_{i+1} - y^0_i\big) \\ \mathbf{F}_{xy} = u_{,y} = \dfrac{1}{2S}\displaystyle\sum_{n=1}^{N} -(u_i + u_{i+1})\big(x^0_{i+1} - x^0_i\big) \\ \mathbf{F}_{yx} = v_{,x} = \dfrac{1}{2S}\displaystyle\sum_{n=1}^{N}(v_i + v_{i+1})\big(y^0_{i+1} - y^0_i\big) \\ \mathbf{F}_{yy} = v_{,y} = \dfrac{1}{2S}\displaystyle\sum_{n=1}^{N} -(v_i + v_{i+1})\big(x^0_{i+1} - x^0_i\big) \end{cases} \tag{10}$$

where u_i and v_i are the displacements along x- and y-axis and I is cyclic with period N, i.e. when $i = N$, $i+1$ is equal to 1. The area of the polygon S was calculated using [31]

$$S = \frac{1}{2}\sum_{n=1}^{N}\big(x^0_i - x^0_{i+1}\big)\big(y^0_{i+1} + y^0_i\big) \tag{11}$$

The partial derivatives $u_{,x}$, $u_{,y}$, $v_{,x}$ and $v_{,y}$ estimated using the Equation 10 were used to calculate the strain with Equation 4.

4. Precision of strain measurements

Source of errors in the calculated strain can arise from the calculation errors of the algorithm and from the measurement errors. Calculation errors arise due to errors inherent in the algorithm for the estimation of the partial derivatives by Equation 10 and from the calculations of the strain by Equations 3 and 4. One source of measurement error arises from the image processing procedure which introduces a discretisation error. It is only possible to measure the position with values corresponding to an integer number of pixels. In our case, 1 pixel corresponded to 0.2 μm. The consequence is that, if the coordinate for the ideal case x_A is equal to 11.68 μm (58.4 pixel), the measured value x_B would be 11.6 μm (58 pixel) and for an ideal value of 11.72 μm (58.6 pixel) the measured coordinate would be 11.8 μm (59 pixel). In addition, there is a measurement error which arises from the limited precision for the measurement of the position of each reference point.

Several arrays of simulated displacement data were prepared to estimate the errors in the calculated strain values.

The first set (Set A) was to evaluate the calculated accuracy of the two algorithms: algorithm 1 (engineering strain calculated using Equation 3) and algorithm 2 (tensor strains calculated using Equation 4). Initial coordinates of the reference points (x_0, y_0) for a non-strained sample were taken as the intersections of the lines of a square grid of size 52×48 μm which had a line spacing of 4 μm. The displacements u and v corresponding to the initial data were calculated from the Westergard equations for plane stress under Mode I load [32]:

$$\begin{aligned} u &= \frac{K_I}{\mu}\sqrt{\frac{\rho}{2\pi}}\cos\frac{\theta}{2}\left(\frac{1-\nu}{1+\nu} + \sin^2\frac{\theta}{2}\right) \\ v &= \frac{K_I}{\mu}\sqrt{\frac{\rho}{2\pi}}\sin\frac{\theta}{2}\left(\frac{2}{1+\nu} + \cos^2\frac{\theta}{2}\right) \end{aligned} \tag{12}$$

The strain corresponding to these displacements is given by [32]:

$$\begin{aligned} \varepsilon_{xx} &= \frac{K_I}{E}\sqrt{\frac{1}{2\pi\rho}}\cos\frac{\theta}{2} \\ &\quad\times\left((1-\nu) - (1+\nu)\sin\frac{\theta}{2}\sin\frac{3\theta}{2}\right) \\ \varepsilon_{yy} &= \frac{K_I}{E}\sqrt{\frac{1}{2\pi\rho}}\cos\frac{\theta}{2} \\ &\quad\times\left((1-\nu) + (1+\nu)\sin\frac{\theta}{2}\sin\frac{3\theta}{2}\right) \end{aligned} \tag{13}$$

where K_I the stress intensity factor was taken to be 50 MPa$\sqrt{\text{m}}$, u and v are the displacements along the x- and y-axes, ρ and θ are the polar coordinates with the crack tip as the origin, μ is the shear modulus, E is Young's modulus of elasticity and ν is Poisson's ratio. The coordinates of the reference points on the deformed sample were calculated as (x_A, y_A), where $x_A = x_0 + u$ and $y_A = y_0 + v$. This set of model data was used to evaluate the accuracy of the calculations for the ideal case, where the position of each reference points was known to the limits of representation in the computer (1×10^{-45}).

The second set of data (Set B) was used to evaluate the influence of the dicretisation error on the accuracy of the strain calculations. To generate the second data set, the data from the first set were modified to correct the coordinate positions to reflect the discretisation error with the following equations:

$$\begin{aligned} x_B &= [(x_A + \delta/2)/\delta]\cdot\delta \\ y_B &= [(y_A + \delta/2)/\delta]\cdot\delta \end{aligned} \tag{14}$$

where δ is the length corresponding to 1 pixel and $[a]$ represents the integer part of a (bracket function).

A third series of 12 data sets (Series C) was used to examine the combined influence of the discretisation error and the finite precision of the measurements of each data point. For each point in set C_i the coordinates were calculated by

$$\begin{aligned} x_{C_i} &= [(x_A + \xi_I + \delta/2)/\delta]\cdot\delta \\ y_{C_i} &= [(y_A + \psi_I + \delta/2)/\delta]\cdot\delta, \end{aligned} \tag{15}$$

where the random errors values ξ_i and ψ_i were generated to satisfy the two variable Gaussian distribution:

$$f(\xi_i, \psi_i) = \frac{1}{2\pi\sigma^2} \exp\left(-\frac{\xi_i^2 + \psi_i^2}{\sigma^2}\right), \qquad (16)$$

where f is the probability density, ξ_i and ψ_i are the errors in the positions for each reference point in i th data set C_i and σ is the standard deviation of the noise taken to be 0.25 μm. Parameters of the normal distribution were chosen to be consistent with the precision of the coordinate measurements in our experiments.

These procedures were used to calculated the following: (1) the initial coordinates of each reference point (x_0, y_0), (2) the coordinates of each reference point on the strained sample ($x_{A,}$ y_A) calculated with the Equation 12 (Set A), (3) coordinates modified according to the discretisation of the measurements (x_B, y_B) using Equation 14 (Set B) and (4) the coordinates which had combined influence of the discretisation error and the finite precision of the measurements according to Equation 15 (series C). Strain from these sets of data were calculated with the Equation 3 (Algorithm 1) and Equation 4 (Algorithm 2). These strain values were compared with the model strain values ε_M calculated using the equation 13. Absolute ($\Delta\varepsilon$) and relative errors (Sr) were calculated as $\Delta\varepsilon_{A,B,C} = \varepsilon_{A,B,C} - \varepsilon_M$ and $Sr_{A,B,C} = \varepsilon_{A,B,C}/\varepsilon_M$, where $\varepsilon_{A,B,C}$ are the strain values calculated from data sets A, B or C.

The strain calculated for the ideal case (Set A) is represented in Fig. 10. Both algorithms yielded a strain distribution similar to the model. For most parts of the strain map for distances greater than 8 μm from the crack tip, the absolute errors for both algorithms were smaller or equal $\pm$0.01. The relative error (Fig. 11a and b) also indicated good performance of the algorithms for distances greater than 8 μm from the crack tip, where the relative error was less then 10% of the measured value. In the area closer than 5 μm to the crack tip the errors were very large, reaching values of more then 50%. This is the region of the strain singularity, where the model strain goes to infinity. It is not surprising that such a strain distribution cannot be reproduced from a grid with a 4 μm line spacing.

Discretisation error altered the shape of the strain distribution. However, the size of the zones with the same strain values remained in a relatively good agreement with the model data.

The calculated values could be presented as $\varepsilon_c = \varepsilon_m + \Delta_s \pm \Delta_r$, where $\varepsilon_c, \varepsilon_m$ are the calculated and model strain value, respectively and Δ_s and Δ_r, are systematic and random calculation errors. Average random (Δ_r) and systematic (Δ_s) calculation errors averaged over all points at distances grater than 5 μm from the crack tip provide a quantitative characteristics of

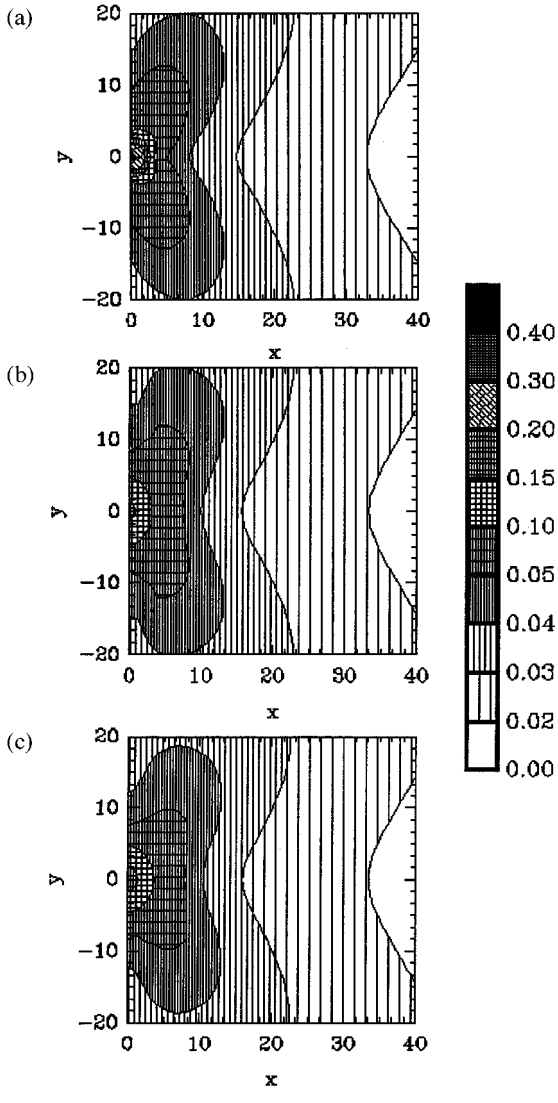

Figure 10 ε_{yy} strain distribution calculated for an ideal case. (a) is model strain distribution, (b) is the strain distribution calculated from data A with algorithm 2 and (c) is the strain distribution calculated from data A with algorithm 1.

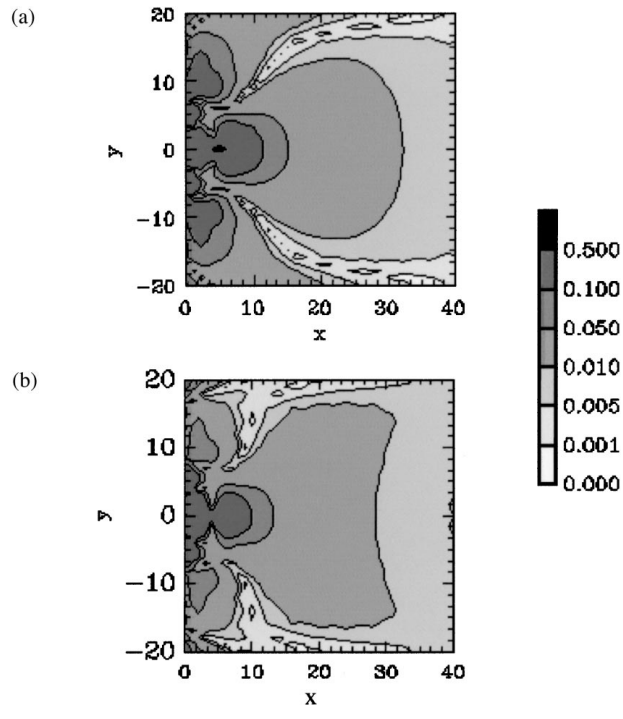

Figure 11 Relative error in the calculations of ε_{yy} strain. (a), (b) are the absolute errors in strain calculations by algorithm 1 and algorithm 2 respectively, an ideal case (data set A).

the performance of each algorithm. Strain values calculated at points closer than 5 μm were excluded from the error analysis because both algorithms produced a large error at the very vicinity of the crack tip even for the ideal case (Set A) as described above. The parameters of the error distributions for all considered points of each data set were determined assuming that the error distribution satisfies normal Gaussian distribution $f(\alpha) = \frac{1}{\sqrt{2\pi}\sigma}\exp(-\frac{\alpha_i^2}{2\sigma^2})$, where $\alpha = \varepsilon_c - \varepsilon_m$. The average random error, Δ_r was calculated from the error distribution and was taken to be 2σ (95% confidence interval), where σ is the standard deviation of the calculation errors. The systematic error Δ_s was taken to be equal to the parameter α from the error distribution function. The performance of the algorithms is characterised in Table I. Both algorithms performed satisfactorily. However, Algorithm 2 provided slightly better handling of discretisation and measurement errors.

Both algorithms showed high sensitivity to random noise (series C, 1 set of data). The strain distributions obtained from just one set of noisy data significantly differed from the model (Fig. 12a and b). However, averaging over 12 independent noisy data sets from series C resulted in reasonable agreement between calculated and model strain distribution (Fig. 12c and d).

The average random error decreased significantly with the number of independent measurements (Fig. 13). To improve the reliability of the results and decrease Δ_r from ± 0.06 to ± 0.02 requires averaging over 6 independent measurements for Algorithm 2 and over 12 data set for Algorithm 1. Thus, Algorithm 2, based on Equation 4, demonstrated better precision and was chosen for the treatment of the experimental data.

5. Conclusions

A technique for ESEM measurements of the crack tip strain field was developed.

- A stressing stage for the ESEM was manufactured which was capable of applying loads up to 40 kN in constant displacement K_I mode.
- Procedures were developed for introducing a system of reference points on the sample surface.
- Procedures were developed for processing the images to obtain coordinates of the reference points before and after loading.
- Algorithms were established to calculate the strain values.
- An evaluation of the calculation precision was performed to ensure correct interpretation of the experimental data.

TABLE I Average random (Δ_r) and systematic (Δ_s) calculation errors

	Ideal data (set A)		Discrete data (set B)		Noisy data (series C, all 12 data sets)	
	Algorithm 1	Algorithm 2	Algorithm 1	Algorithm 2	Algorithm 1	Algorithm 2
Δ_s	0.001	0.001	0.0036	0.0028	0.0042	0.0029
Δ_r	0.0018	0.0018	0.0098	0.0098	0.0172	0.0163

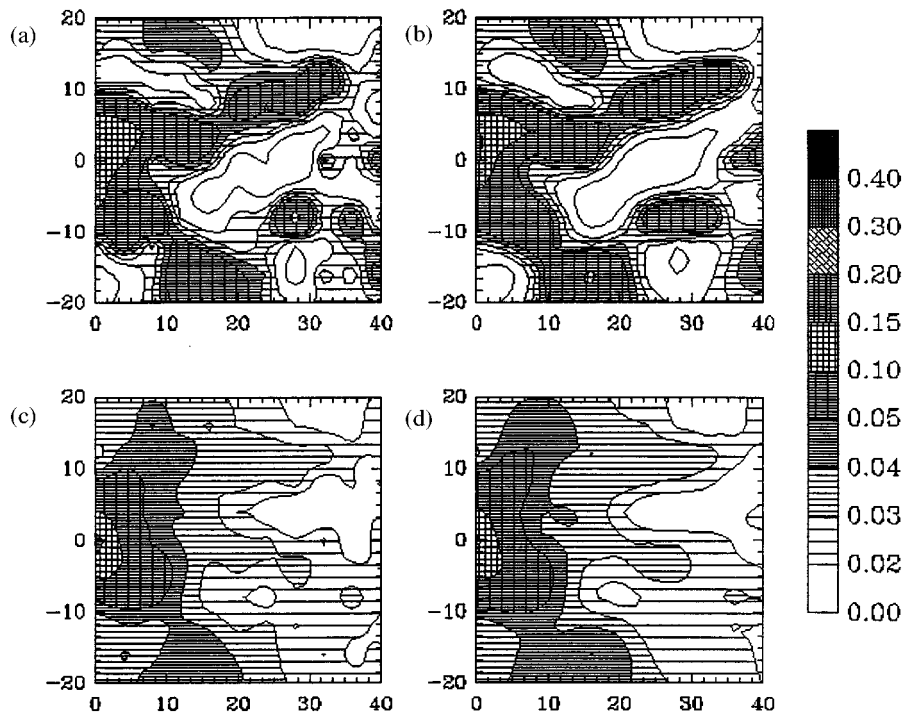

Figure 12 ε_{yy} strain distribution calculated from noisy data. (a), (b) are the strain distribution calculated from one noisy data set from series C with algorithm 1 and algorithm 2, (c) and (d) are the strain distribution averaged over 12 noisy data sets from series C (algorithm 1 and algorithm 2).

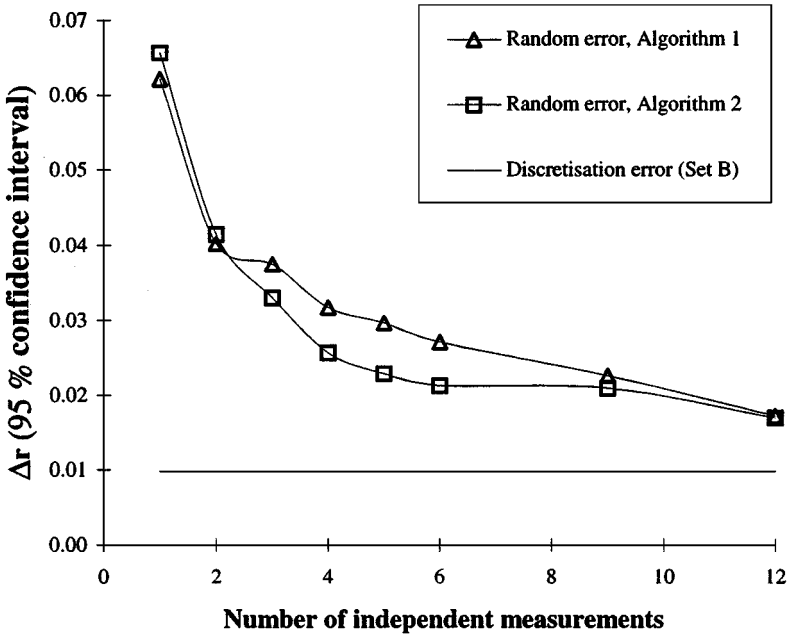

Figure 13 Influence of the number of independent measurements on the precision of the strain calculations.

- For the current experimental arrangement the strain mapping technique was capable of measuring the strain distribution at distances greater than 5 μm from the crack tip with a precision in strain values of ± 0.02.

Acknowledgement

This work was supported by the Australian Research Council.

References

1. A. ATRENS and Z. F. WANG, *Materials Forum* **19** (1995) 9.
2. S. JIN and A. ATRENS, *Applied Physics A* **42** (1987) 149.
3. *Idem., ibid.* **50** (1990) 287.
4. A. S. LIM and A. ATRENS, *ibid.* **54** (1992) 500.
5. *Idem., ibid.* **53** (1992) 273.
6. Z. F. WANG and A. ATRENS, *Metall. and Mater. Trans. A.* **27A** (1996) 2686.
7. A. ATRENS, Z. F. WANG, N. KINAEV, D. R. COUSENS and J. Q. WANG, 13 ICC, Melbourne, paper 233.
8. Z. F. WANG and A. ATRENS, *J Mater. Sci.* **33** (1998) 405.
9. A. OEHLERT and A. ATRENS, *Materials Forum* **17** (1993) 415.
10. *Idem., Corrosion Science* **38** (1996) 1159.
11. R. M. RIECK, A. ATRENS and I. O. SMITH, *Met. Trans.* **20A** (1989) 889.
12. A. ATRENS, C. C. BROSNAN, S. RAMAMURTHY, A. OEHLERT and I. O. SMITH, *Measurement Science and Technology* **4** (1993) 1281.
13. S. RAMAMURTHY and A. ATRENS, *Corrosion Science* **34** (1993) 1385.
14. J. SALMOND and A. ATRENS, *Scripta Metallurgica et Materialia* **26** (1992) 1447.
15. A. OEHLERT and A. ATRENS, *Acta Metallurgica et Materialia* **42** (1994) 1493.
16. G. L. DANILATOS, *Advances in Electronics and Electron Physics* **71** (1988) 110.
17. R. C. McCLUNG and D. L. DAVIDSON, *Engineering Fracture Mech.* **39** (1991) 113.
18. L. ALLAIS, M. BORNERT, T. BERTHEAU and D. CALDEMAISON, *Acta Metall. Mater.* **42** (1994) 3865.
19. S. YONGQI, S. CORLETTO, W. L. BRADLEY and J. TIAN, *Exp. Mech.* **36** (1996) 193.
20. Y. L. LIU and G. FISCHERR, *Scripta Mater.* **36** (1997) 1187.
21. A. NAGY, J. B. CAMPBELL and D. L. DAVIDSON, *Rev. Sci. Instrum.* **55** (1984) 778.
22. O. Ø. MOURITSEN and B. L. KARIHALOO, *Advances in Fracture Research* (1997) 1437.
23. D. G. ATTWOOD and P. M. HAZZLEDINENE, *Metals* **9** (1976) 483.
24. E. A. FRANKE, D. J. WENZEL and D. L. DAVIDSON, *Rev. Sci. Instrum.* **62** (1991) 1270.
25. D. L. DAVIDSON, in "Experimental Techniques in Fracture," N.-Y., VCH, edited by. J. S. Epstein (1993) p. 41.
26. K. HATANAKA, T. FUJIMITSU and H. INOUE, *Exp. Mech.* **32** (1992) 211.
27. K. ANDERSEN and B. HÜBNER, *Exp. Mech.* **32** (1992) 96.
28. N. KINAEV, J. V. NAILON, D. R. COUSENS, R. MILLER and P. J. R. UWINS, 14 ACEM, Gold Coast, p. 38.
29. H. R. SMITH and D. E PIPER, in "SCC in High Strength Steels and Titanium and Aluminium Alloys," edited by B. F. Brown (NRL, Washington DC, 1972) p. 17.
30. E. CHARYSHKIN, N. N. KINAEV, M. WATERWORTH, D. R. COUSENS, N. CALOS, T. BOSTROM and A. ILYUSHECHKIN, *Phys. Stat. Sol. (a)* **154** (1996) 43.
31. D. ZWILLINGER (ed.), "Standard Mathematical Tables and Formulae" (CRC Press, NY, 1996) p. 270.
32. D. J. UNGER, "Analytical Fracture Mechanics" (Academic Press, London, 1995) p. 26.

Received 21 October
and accepted 18 November 1998